

---

# Specular transmission and diffuse reflection in phonon scattering at grain boundary

ZHUN-YONG ONG<sup>1</sup>

<sup>1</sup> *Institute of High Performance Computing, A\*STAR, Singapore 138632, Singapore*

PACS 63.20.kp – Phonon-defect interactions

**Abstract** – It is widely assumed in the literature that the specularity parameters for phonon transmission (forward scattering) and reflection (backward scattering) at a boundary are identical, i.e., the statistical distributions of the transition probabilities between an incident phonon and the range of outgoing phonon modes are the same for both transmission and reflection. However, it is hypothesized by Li and McGaughey that separate specularity parameters are needed to describe the behavior of transmitted and reflected phonons in superlattices and polycrystalline materials correctly. We test this hypothesis by analyzing the mode-resolved specularity parameters computed separately for transmission and reflection processes at a graphene grain boundary. Our results show that backward scattering is considerably more diffuse than forward scattering at most frequencies and polarizations, providing strong evidence for Li and McGaughey’s hypothesis, and shed new light on how surfaces and interfaces modify phonon transport within and between domains in nanostructured materials.

---

**Introduction.** – One of the main factors limiting the lattice thermal conductivity of nanostructures (e.g. Si nanowires [1,2]) and polycrystalline materials is boundary scattering at free surfaces and solid-solid interfaces [3,4], a process which impedes phonon propagation by dissipating phonon momentum. The degree of momentum dissipation per scattering event depends on its specularity and is characterized by the specularity parameter ( $\mathcal{P}$ ) which satisfies the condition  $0 \leq \mathcal{P} \leq 1$  and varies with boundary morphology as well as the momentum, frequency and branch of the incident phonon [5,6].

In perfectly specular scattering ( $\mathcal{P} = 1$ ), the incident phonon is either reflected or transmitted specularly with no loss of transverse momentum (momentum in the direction parallel to the boundary) while in perfectly diffusive scattering ( $\mathcal{P} = 0$ ) or the so-called *Casimir* limit, the incoming phonon energy is redistributed uniformly over the entire spectrum of outgoing phonon channels with total loss of transverse momentum due to randomization of the phonon trajectory [7]. In reality, most boundary scattering processes are neither fully specular nor diffuse, i.e.,  $0 < \mathcal{P} < 1$ , even for a rough boundary because the scattering amplitudes, which determine the transitions between the incoming and outgoing phonon states, have a nonuniform distribution. Hence, the determination of the specularity parameters can provide an accurate quantification

of the momentum loss and thermal conductivity reduction from boundary scattering.

In the case of a solid-solid interface, a phonon is partially forward-scattered (i.e. transmitted) across the boundary and partially backward-scattered (i.e. reflected) into the original bulk lattice, resulting in thermal resistance in the directions normal and parallel to the boundary. In the normal direction, momentum is lost directly as a result of incomplete transmission across the interface while in the parallel direction, transverse momentum is lost through diffuse scattering at the boundary. In superlattices where there are multiple interfaces [8,9], the first process creates thermal resistance in the cross-plane direction while the second process reduces thermal conductivity in the in-plane direction.

It is widely assumed that in the second process, transverse momentum dissipation is similar for phonon transmission and reflection [7,10–14] so that the degree of randomization for transmitted phonons is the same as that for reflected phonons. In many models where the scattering is only partially random, [10–14] the same specularity parameter is used to determine the phonon distributions on both sides of the interface. In the diffuse mismatch model, [15] the transmitted and reflected phonons are completely randomized. However, it has been suggested by Li and McGaughey [3] that phonon reflection

is much more diffuse and sensitive to boundary roughness than phonon transmission, i.e., the incident phonon is spread more diffusely over the outgoing (reflected) phonon channels on the same side of the boundary than it is over the outgoing (transmitted) phonon channels on the other side as depicted in Fig. 1, and thus, greater transverse momentum dissipation results from reflection than transmission. This difference in the diffuseness of scattering draws further support from Ref. [16] where Shi, Lowe and Craster analyzed the elastic scattering of waves in an elastodynamic model of the Si-Ge interface using the Kirchhoff approximation [17] (KA) and concluded within the validity of the KA and the continuum limit that the reflection and transmission of low-frequency (sub-THz) waves can have different dependence on interface roughness when the correlation length of the boundary is large. Therefore, the directional dependence of boundary scattering implies that two specularly parameters, one for reflection ( $\mathcal{P}^-$ ) and the other for transmission ( $\mathcal{P}^+$ ), are needed to describe phonon scattering at the interface of two media.

If proven to be true, this distinction between the reflection and transmission specularly can potentially resolve some of the puzzles in nanoscale thermal transport involving phonon interactions with surfaces and interfaces [3]. For example, a specularly of  $\mathcal{P} \approx 0$  is needed to interpret the experimental characterization of thermal transport in freestanding nanowires and thin films which have only phonon reflection from free surfaces [18, 19] while a significantly larger average specularly parameter is needed to model the in-plane thermal conductivity of superlattices where there is both phonon transmission and reflection [20], a discrepancy that can be explained by assuming distinct specularly parameters for reflection and transmission and that the transmission specularly is greater than the reflection specularly, i.e. the transmitted phonons are less randomized than the reflected phonons ( $\mathcal{P}^+ \gg \mathcal{P}^-$ ). However, the evidence supporting distinct specularly parameters for phonon reflection and transmission remains only circumstantial as it is based on experimental data interpretation [3]. Even in simulations, the direct evaluation of  $\mathcal{P}^+$  and  $\mathcal{P}^-$ , which are not defined precisely for individual phonon modes, is constrained by the difficulty in computing the boundary scattering amplitudes.

In this article, we show that phonon transmission is less diffuse than phonon reflection over most of the Brillouin zone (BZ), highlighting the need for distinct specularly parameters to characterize phonon reflection and transmission. To accomplish this, we define and directly evaluate the *mode-resolved* specularly parameters for phonon reflection ( $\mathcal{P}^-$ ) and transmission ( $\mathcal{P}^+$ ) at a (32,32)|(56,0) GB between armchair and zigzag-edge graphene [21]. Our approach, which is facilitated by the recently developed *S*-matrix method [22] for calculating the *exact* scattering amplitudes, is based on the analysis of the statistical spread of transition probabilities and is elaborated in an earlier paper [23] where the total specularly ( $\mathcal{P}$ ) of the

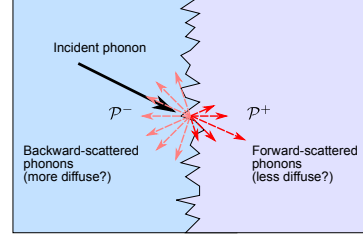


Figure 1: Illustration of the transmission and reflection specularly parameters ( $\mathcal{P}^+$  and  $\mathcal{P}^-$ ) for phonon scattering at a solid-solid interface.  $\mathcal{P}^+$  and  $\mathcal{P}^-$  measure the degree of randomization in the forward and backward-scattered phonons, respectively.

(32,32)|(56,0) GB is studied. We choose this GB structure as our model system because armchair and zigzag-edge graphene have a similar but not necessarily identical number of incoming phonon channels at most frequencies, i.e.,  $N_{AC}(\omega) \approx N_{ZZ}(\omega)$  where  $N_{AC}$  ( $N_{ZZ}$ ) is the number of incoming phonon channels in armchair-edge (zigzag-edge) graphene at frequency  $\omega$ , allowing us to exclude this as a factor affecting the specularly. In our analysis of the scattering amplitudes, we introduce an expression for estimating the normalized transmission and reflection specularly parameters ( $P_n^+$  and  $P_n^-$ ) of the  $n$ -th incoming phonon ( $n = 1, \dots, N$  for  $N = N_{AC} + N_{ZZ}$ ) and discuss how  $P_n^+$  and  $P_n^-$  vary with phonon frequency ( $\omega_n$ ), momentum ( $\mathbf{k}_n$ ) and branch ( $\nu_n$ ). We also compute the mode-resolved transmission probability ( $\mathcal{T}_n$ ) and show that its distribution in the BZ is highly similar to that of the transmission specularly  $P_n^+$ .

**Graphene grain boundary and *S*-matrix calculation.** – Although the details of the generation and optimization of the graphene GB structures in our simulation are identical to those in Ref. [23], we give a brief overview of the method here with further details in the Supplemental Material [24]. We construct the (32,32)|(56,0) graphene GB model from the two lowest-energy (4,4)|(7,0) GB configurations (GB-II and GB-III) in Ref. [21] found using the *ab initio* random structure searching method [25]. Each (32,32)|(56,0) GB configuration comprises  $l = 8$  (4,4)|(7,0) GB's, a permutation of GB-II's and GB-III's, forming a continuous line of pentagon-heptagon defect pairs as shown in Fig. 2(a). In total, there are  $2^l = 256$  unique GB configurations. We set the direction of the phonon flux and the GB to be parallel to the  $x$  and  $y$  axis, respectively, and impose periodic boundary conditions in the  $y$  direction, resulting in the discretization of the transverse component of the wave vector ( $k_y$ ) with the step size of  $\Delta k_y = \frac{2\pi}{L_y}$  where  $L_y$  is the width of the GB. We note here that the number of modes is finite because of the nonzero  $\Delta k_y$  associated with the finite GB width. The empirical Tersoff potential [26], with parameters from Ref. [27], is used to model the C-C interatomic forces. The program GULP [28] is

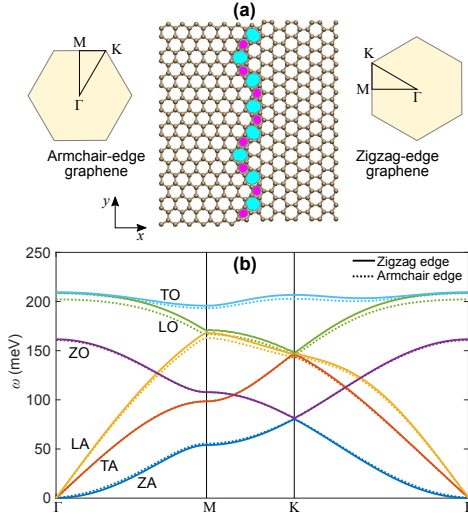


Figure 2: **(a)** Depiction of the GB between armchair and zigzag-edge graphene. The different graphene lattices (armchair-edge vs. zigzag-edge) are referred according to their edge orientation in the  $y$  direction. **(b)** Bulk phonon dispersion curves of armchair (dotted lines) and zigzag-edge (solid lines) graphene along the major BZ symmetry points and labeled according to branch [29]. The small differences in the phonon dispersion are due to the tensile strain in armchair-edge graphene in the  $y$  direction. Both the TA and ZA phonon dispersion curves have an inverted Dirac cone at the  $K$  point.

used to optimize each GB configuration and to generate its interatomic force constant (IFC) matrices  $\mathbf{H}_{\text{CL}}$ ,  $\mathbf{H}_{\text{C}}$  and  $\mathbf{H}_{\text{CR}}$  needed for the  $S$ -matrix calculations. We also compute the IFC matrices  $\mathbf{H}_{\text{L}}^{00}$  and  $\mathbf{H}_{\text{L}}^{01}$  ( $\mathbf{H}_{\text{R}}^{00}$  and  $\mathbf{H}_{\text{R}}^{01}$ ) describing the bulk phonons in the armchair-edge (zigzag-edge) graphene on the left (right) side of the GB, with the phonon dispersion curves along the high-symmetry directions shown in Fig. 2(b).

At each frequency  $\omega$ , we compute an  $N(\omega) \times N(\omega)$  matrix  $\mathbf{S}(\omega)$  for each GB configuration, where  $N(\omega) = N_{\text{AC}}(\omega) + N_{\text{ZZ}}(\omega)$  is the number of phonon scattering channels, using the IFC matrices  $\mathbf{H}_{\text{CL}}$ ,  $\mathbf{H}_{\text{C}}$ ,  $\mathbf{H}_{\text{CR}}$ ,  $\mathbf{H}_{\text{L}}^{00}$ ,  $\mathbf{H}_{\text{L}}^{01}$ ,  $\mathbf{H}_{\text{R}}^{00}$  and  $\mathbf{H}_{\text{R}}^{01}$ , based on the method described in Refs. [22, 23]. Details of the calculation of the  $S$  matrix are given in the Supplemental Material [24]. The individual  $S$ -matrix element  $[\mathbf{S}(\omega)]_{mn} = S(\mathbf{k}_m, \mathbf{k}'_n)$  gives the scattering amplitude from the incoming phonon channel with wave vector  $\mathbf{k}'_n$  and branch index  $\nu'_n$  to the outgoing phonon channel with wave vector  $\mathbf{k}_m$  and branch index  $\nu_m$ . The transition probability matrix  $\mathbf{W}(\omega)$  is obtained by taking the configurational ensemble average, taken over all 256 possible GB configurations and denoted by  $\langle \dots \rangle$ , of the absolute square of the  $S$ -matrix elements [23], i.e.,  $[\mathbf{W}(\omega)]_{mn} = \langle |[\mathbf{S}(\omega)]_{mn}|^2 \rangle$ .

**Definition of specularity parameters and transmission coefficient.** – From  $\mathbf{W}(\omega)$ , we estimate the normalized total specularity parameter of the  $n$ -th in-

coming phonon [23] using the expression:

$$P_n^{\text{total}}(\omega) = \frac{\sqrt{\sum_{k_y} \phi_n(k_y)^2}}{\sum_{k_y} \phi_n(k_y)}, \quad (1)$$

where  $k_y$  is the discretized transverse wave vector and  $\phi_n(k_y) = \sum_{m=1}^{N(\omega)} [\mathbf{W}(\omega)]_{mn} \delta_{k_{y,m}, k_y}$  is the sum of the probability of the  $n$ -th incoming phonon mode scattering to outgoing channels with the transverse wave vector  $k_y$ . Equation (1) is analogous to the inverse participation ratio used in localization theory [30] but measures the localization of scattering in  $k_y$  instead of real space. In perfectly specular scattering,  $k_y$  is conserved so that  $\phi_n(k_y) = 1$  for  $k_y = k'_{n}$  and 0 otherwise. Hence, Eq. (1) yields  $P_n^{\text{total}}(\omega) = 1$  for perfectly specular scattering and  $\lim_{N(\omega) \rightarrow \infty} P_n^{\text{total}}(\omega) = 0$  for totally diffuse scattering. By grouping together the probabilities of the outgoing channels with the transverse wave vector  $k_y$  in  $\phi_n(k_y)$ , we account for the effects of mode conversion in specular scattering.

The transmission coefficient or probability [31] of the  $n$ -th incident phonon mode, equal to the sum of its transition probabilities to outgoing forward-scattered phonon modes, is given by

$$\mathcal{T}_n(\omega) = \sum_{m=1}^{N(\omega)} [\mathbf{W}(\omega)]_{mn} \Theta(v_{x,m} v'_{x,n}) \quad (2)$$

where  $v'_{x,n}$  ( $v_{x,m}$ ) denotes the group velocity component in the  $x$ -direction of the  $n$ -th incoming ( $m$ -th outgoing) phonon mode and  $\Theta(\dots)$  represents the Heaviside step function. The  $\Theta(v_{x,m} v'_{x,n})$  term in the summand in Eq. (2), which equals unity (zero) for outgoing phonon channels associated with forward (backward) scattering, eliminates the transition probability contributions from phonon reflection in Eq. (2). We use the Heaviside step function in a similar manner in our definition of the normalized transmission and reflection specularity parameters ( $P_n^+$  and  $P_n^-$ ):

$$P_n^{\pm}(\omega) = \begin{cases} \frac{\sqrt{\sum_{k_y} \phi_n^{\pm}(k_y)^2}}{\sum_{k_y} \phi_n^{\pm}(k_y)} & \text{if } \sum_{k_y} \phi_n^{\pm}(k_y) > 0 \\ 0 & \text{otherwise} \end{cases} \quad (3)$$

where  $\phi_n^{\pm}(k_y) = \sum_{m=1}^{N(\omega)} [\mathbf{W}(\omega)]_{mn} \delta_{k_{y,m}, k_y} \Theta(\pm v_{x,m} v'_{x,n})$  is the sum of the probability of the  $n$ -th incoming phonon mode scattering to outgoing channels with the transverse wave vector  $k_y$  in the forward (+) or backward (−) direction, so that  $\phi_n(k_y) = \phi_n^+(k_y) + \phi_n^-(k_y)$ . The denominator in Eq. (3) corresponds to the total transmission (+) or reflection (−) probability. Equation (3) measures the scattering localization of the transmitted or reflected phonon modes, with  $P_n^+(\omega) = 1$  ( $P_n^-(\omega) = 1$ ) for specular transmission (reflection), i.e., if the forward (backward) scattering processes conserve the transverse wave vector, and  $\lim_{N(\omega) \rightarrow \infty} P_n^+(\omega) = 0$  ( $\lim_{N(\omega) \rightarrow \infty} P_n^-(\omega) = 0$ ) if the

forward (backward) scattering process is totally diffuse. Unlike Eq. (1),  $P_n^\pm(\omega)$  allows us to distinguish between the degree of specularity in transmission (forward scattering) and reflection (backward scattering).

**Relationship between transmission probability and total specularity parameter.** – We compute  $\mathcal{T}_n$ ,  $P_n^{\text{total}}$ ,  $P_n^+$  and  $P_n^-$  from Eqs. (1)-(3) over the discrete frequency range  $\omega = m\omega_0$  for  $m = 1$  to 25 and  $\omega_0 = 10^{13}$  rad/s (6.58 meV) in armchair-edge graphene. At each frequency point  $\omega$ , we have a set of  $N(\omega)$  bulk phonon modes corresponding to the incoming phonon channels, which we enumerate from  $n = 1$  to  $N(\omega)$ . Thus, by sweeping over the entire frequency range, we obtain the mode-resolved transmission and specularity parameters over the entire Brillouin zone (BZ) in Fig. 3. We associate with the  $n$ -th phonon mode a 2-dimensional wave vector  $\mathbf{k}_n$  and a branch index  $\nu_n$  which can be flexural acoustic (ZA), transverse acoustic (TA) or longitudinal acoustic (LA). The optical phonon branches are ignored in our study while the corresponding results for zigzag-edge graphene are given in the Supplemental Material [24].

Figures 3(a) to (c) show the mode-resolved  $\mathcal{T}_n$  distribution in the first BZ for each phonon branch (ZA, TA or LA). We observe that  $\mathcal{T}_n$  is near-isotropic, showing no significant directional dependence for all branches except for modes that are close to the BZ edge. In spite of the 30-degree tilt between armchair- and zigzag-edge graphene, there is no critical angle for transmission and total internal reflection like that exhibited for interfaces between two dissimilar materials (e.g. the graphene/ $h$ -BN interface [32]). The near-isotropic  $\mathcal{T}_n$  distribution and absence of total internal reflection are attributed to the similar acoustic impedance between armchair- and zigzag-edge graphene in the continuum (long-wavelength) limit and are consistent with the acoustic mismatch model (AMM) [15] which predicts that  $\mathcal{T}_n \sim 1$  in the continuum (long-wavelength) limit for the acoustically similar materials.

However, we also observe discrepancies with the AMM. In Figs. 3(a) to (c), the ZA phonon  $\mathcal{T}_n$  decreases as we approach the BZ center or edges while the TA and LA phonon  $\mathcal{T}_n$  converges to unity at the BZ center and decreases as one approaches the edges. The increasing LA and TA phonon transparency in the  $\omega \rightarrow 0$  limit is consistent with the AMM and agrees with the findings from wave-packet simulations [33,34] that long-wavelength phonons are more easily transmitted as they are less sensitive to the crystallographic discontinuity. On the other hand, the reduced  $\mathcal{T}_n$  for long-wavelength ZA phonons suggests that they may be more easily scattered by the GB. To investigate this further, we plot  $\mathcal{T}_n$  of the low-frequency ZA phonons over the frequency range of  $\omega = 0.1\omega_0$  to  $2\omega_0$  for armchair and zigzag-edge graphene in Fig. 4. The results agree with our findings at high frequencies showing  $\mathcal{T}_n$  decreasing with frequency and may be connected to the more pronounced anisotropy of the ZA phonon dis-

persion in armchair-edge graphene, which is strained in the  $y$  direction, relative to that in zigzag-edge graphene. As a result of this low-frequency anisotropy, there is an imbalance in the number of ZA phonon modes between the armchair and zigzag-edge graphene at low frequencies, with proportionally fewer modes in the former than in the latter. For instance, at  $\omega = 0.1\omega_0$  the lowest simulated frequency, there is only one available ZA phonon mode in armchair-edge graphene and five in zigzag-edge graphene. We have also performed the same calculations for a more structurally ordered grain boundary constructed from GB-II subunits and the results, shown in the Supplementary Material, [24] also exhibit a qualitatively similar decrease in  $\mathcal{T}_n$  with frequency.

To quantify scattering by the GB, we plot in Figs. 3(d) to (f) the mode-resolved total specularity  $P_n^{\text{total}}$  distribution [Eq. (1)] in the first Brillouin Zone (BZ) for each phonon polarization (ZA, TA or LA). We notice immediately a close similarity between the  $\mathcal{T}_n$  and  $P_n^{\text{total}}$  distribution for the TA and LA phonons:  $\mathcal{T}_n$  and  $P_n^{\text{total}}$  converge to unity as one approaches the BZ center. This implies that if the TA or LA phonon is less diffusely scattered by the GB, its transmission across the GB increases correspondingly. A similar trend is observed for TA and LA phonons in zigzag-edge graphene.

Conversely, Fig. 3(d) shows that the ZA phonon  $P_n^{\text{total}}$  decreases in the long-wavelength limit, consistent with the trend observed for the ZA phonon  $\mathcal{T}_n$  in Fig. 3(a) and confirming previous observations [35–37] that long-wavelength ZA phonons are more easily scattered by the GB. In addition, we also observe that total specularity for ZA phonons [Figs. 3(a) and (d)] is significantly smaller than unity even for ZA phonon modes that have  $\mathcal{T}_n \sim 1$  [Figs. 3(a) and (d)]. This suggests that *forward* scattering for the transmitted ZA phonons is diffuse, a phenomenon which may be due to the low-frequency ZA phonon dispersion anisotropy in armchair-edge graphene and the decrease in their group velocities at low frequencies.

**Difference between transmission and reflection specularity distribution.** – To characterize how diffusely scattered the transmitted phonons are, we plot the transmission specularity  $P_n^+$  distribution in Figs. 3(g) to (i). Like in Figs. 3(d) to (f), the  $P_n^+$  distributions are near-isotropic for the ZA, TA and LA phonons. Nonetheless, there is a striking difference between the ZA phonon  $P_n^+$  distribution and the TA/LA phonon  $P_n^+$  distributions: as we approach the BZ center,  $P_n^+$  converges to unity for the TA/LA phonons but not for the ZA phonons. This implies that as the phonon momentum  $k$  decreases, the transmitted TA and LA phonons tend to be more specularly forward-scattered, i.e., the transmitted phonon energy is more concentrated into a single outgoing phonon channel on the other side of the GB. On the other hand, Fig. 3(g) shows that the transmitted ZA phonons are partially diffusive even in the  $\omega \rightarrow 0$  limit. This implies that at low frequencies, the transmitted phonon energy is spread over



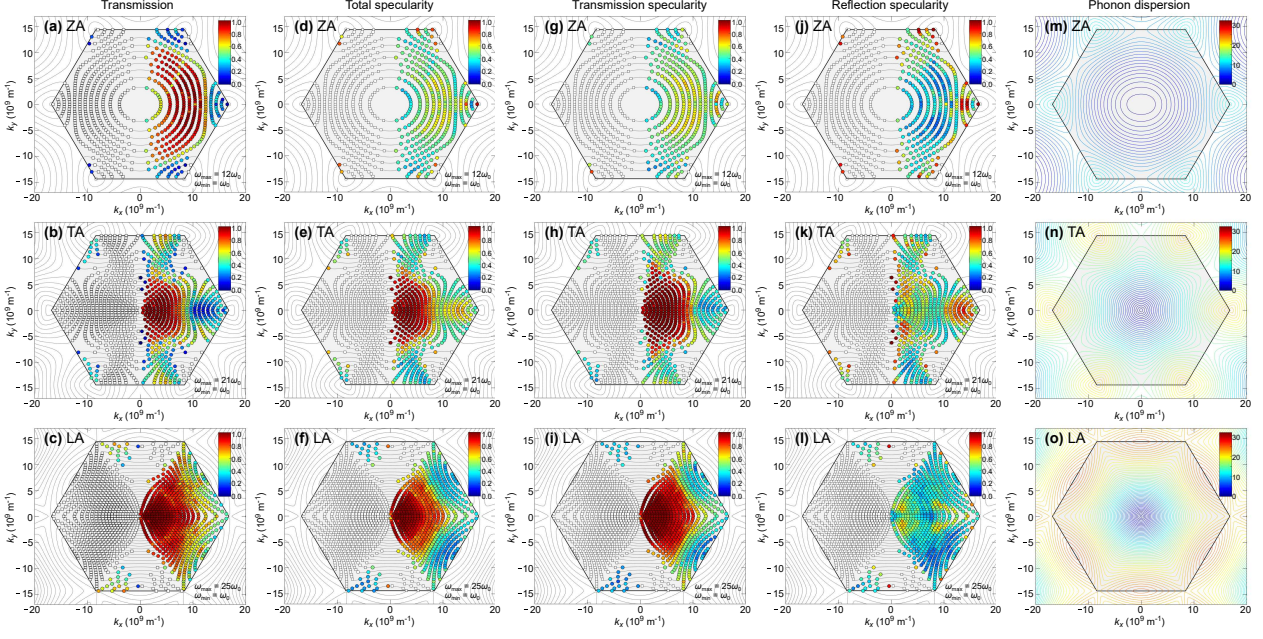


Figure 3: Mode-resolved comparison of (a-c)  $\mathcal{T}_n(\omega)$ , (d-f)  $P_n^{\text{total}}(\omega)$ , (g-i)  $P_n^+(\omega)$ , and (j-l)  $P_n^-(\omega)$  for ZA, TA and LA phonons in armchair-edge graphene at each frequency  $\omega$  point over the frequency range  $\omega = m\omega_0$  for  $m = 1$  to 25 and  $\omega_0 = 10^{13}$  rad/s (6.58 meV). The isofrequency contours at each  $\omega$  are shown using solid gray lines. The modes in the incoming phonon flux are represented by filled circles, colored according to their numerical value as indicated in the color bars, while the modes in the outgoing flux are represented by hollow squares. The (m) ZA, (n) TA and (o) LA phonon dispersions are indicated with color contours in intervals of  $\Delta\omega = \omega_0/2$ .

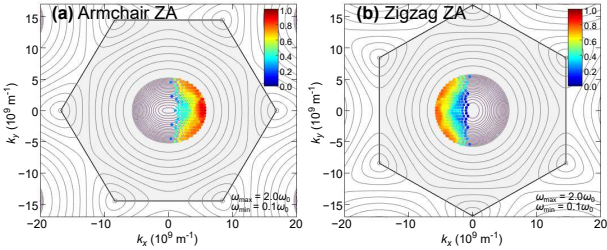


Figure 4: Mode-resolved comparison of  $\mathcal{T}_n(\omega)$  in the low-frequency regime for ZA phonons in (a) armchair and (b) zigzag-edge graphene at each frequency  $\omega$  point over the frequency range  $\omega = 0.1\omega_0$  to  $2\omega_0$  for  $\omega_0 = 10^{13}$  rad/s (6.58 meV) with a frequency step size of  $0.1\omega_0$ . The isofrequency contours at each  $\omega$  at and under  $\omega = 2\omega_0$  are displayed using solid magenta lines at intervals of  $\Delta\omega = 0.1\omega_0$  while the isofrequency contours between  $\omega = 2\omega_0$  and  $\omega = 12\omega_0$  are displayed using solid gray lines at intervals of  $\Delta\omega = \omega_0$ . The modes in the incoming phonon flux are represented by filled circles, colored according to their numerical value as indicated in the color bars.

multiple outgoing phonon channels across the GB, a phenomenon also observed in Ref. [36]. We also notice that the ZA, TA and LA phonons share a similarity where  $P_n^+$  generally decreases as we approach the BZ edges and corners, indicating that shorter wavelength phonons are more diffusely scattered by the GB. In particular, the overall  $P_n^+$

distribution is more similar to the  $\mathcal{T}_n$  distribution than the  $P_n^{\text{total}}$  distribution is.

For comparison with  $P_n^+$  in Figs.3(g) to (i), we plot the reflection specularity  $P_n^-$  distribution in Figs. 3(j) to (l). We observe that  $P_n^- < P_n^+$  as we approach the BZ center ( $\Gamma$  point) with the difference most pronounced for LA phonons, confirming Li and McGaughey's hypothesis. On the other hand, for the transversely polarized TA and ZA phonons, we find that  $P_n^- > P_n^+$  as we approach the BZ corners ( $K$  points), possibly due their inverted Dirac cone-like phonon dispersion at the  $K$  points as seen in Fig. 2(b). The absence of this behavior for the LA phonons suggests that the phonon dispersion plays a critical role in specularity, a phenomenon which needs to be further investigated.

**Role of disorder.** – To analyze the role of disorder in phonon scattering, we compute and plot  $\mathcal{T}_n$ ,  $P_n^{\text{total}}$ ,  $P_n^+$  and  $P_n^-$  in Fig. 5 for a (32,32)|(56,0) graphene GB constructed from only GB-II subunits. Physically, this GB configuration is a regular array of GB-II subunits and less disordered than the earlier GB models comprising a random mix of GB-II and GB-III subunits. In the following discussion, we refer to it as the ordered GB model and the earlier GB models collectively as the disordered GB model. In terms of phonon transmission ( $\mathcal{T}_n$ ), we do not observe any significant difference between the ordered and disordered GB models except in Fig. 5(a) and Fig. 3(a) where the low-frequency ZA phonons at  $\omega = 10^{13}$  rad/s are more

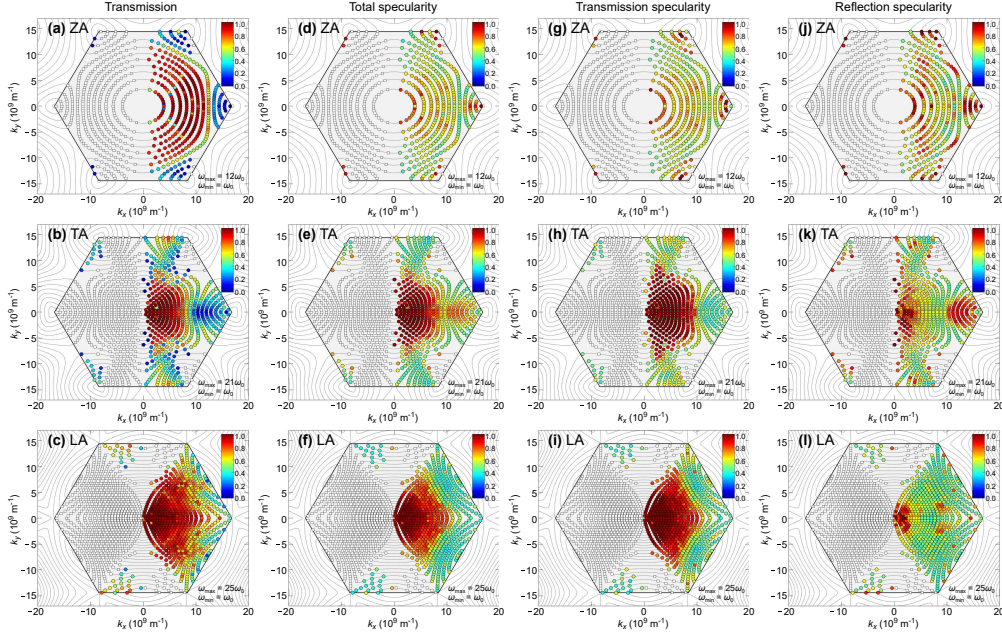


Figure 5: Mode-resolved comparison of (a-c)  $\mathcal{T}_n(\omega)$ , (d-f)  $P_n^{\text{total}}(\omega)$ , (g-i)  $P_n^+(\omega)$ , and (j-l)  $P_n^-(\omega)$  for ZA, TA and LA phonons in armchair-edge graphene at each frequency  $\omega$  point over the frequency range  $\omega = m\omega_0$  for  $m = 1$  to 25 and  $\omega_0 = 10^{13}$  rad/s (6.58 meV) for a (32,32)|(56,0) graphene GB constructed from only GB-II subunits. The isofrequency contours at each  $\omega$  are shown using solid gray lines. The modes in the incoming phonon flux are represented by filled circles, colored according to their numerical value as indicated in the color bars, while the modes in the outgoing flux are represented by hollow squares.

easily transmitted in the ordered GB model. This suggests that the reduction in  $\mathcal{T}_n$  for low-frequency ZA phonons in the disordered GB model is caused by the increased scattering with disorder. We find further support for this explanation by comparing  $P_n^{\text{total}}$ ,  $P_n^+$  and  $P_n^-$  for the ZA phonons in the ordered and disordered GB models. Figures 5(d), (g) and (j) show that  $P_n^{\text{total}}$ ,  $P_n^+$  and  $P_n^-$  are higher for the ordered GB model compared to the results in Figs. 3(d), (g) and (j). We also find that the  $P_n^+$  and  $P_n^-$  distribution for ZA phonons are comparable for the ordered GB unlike the  $P_n^+ > P_n^-$  trend for the disordered GB. For the TA and LA phonons, the difference between the  $P_n^+$  and  $P_n^-$  distribution is less pronounced in the ordered GB especially at low frequencies near the center of the BZ where  $P_n^+$  and  $P_n^-$  are comparable and close to unity. Away from the BZ center, we find that  $P_n^+ > P_n^-$  in the ordered GB model although it is less pronounced than the disordered GB model. This is probably because the ordered GB model does not have a perfectly flat interface as it is impossible to form a commensurate boundary between armchair-edge and zigzag-edge graphene.

**Summary and conclusion.** – We have investigated the difference in specularity between phonon reflection and transmission at a graphene GB. Using the atomistic  $S$ -matrix method, we analyze the phonon transmission probability  $\mathcal{T}_n$  and its relationship to the total, transmission and reflection specularity parameters ( $P_n^{\text{total}}$ ,  $P_n^+$  and  $P_n^-$ ) for the LA, TA and ZA phonons. We find that the  $\mathcal{T}_n$  and  $P_n^+$  distributions are highly similar over the entire Brillouin Zone.

There is a striking difference between  $P_n^+$  and  $P_n^-$ , indicating that the degrees of randomization for the transmitted and reflected phonons are dissimilar. We confirm Li and McGaughey’s hypothesis that  $P_n^+ > P_n^-$  especially nearer the  $\Gamma$  point, with the difference most pronounced for LA phonons, and find that  $P_n^+ < P_n^-$  nearer the  $K$  point for TA and ZA phonons, possibly because of their inverted Dirac cone-like phonon dispersion. Our results show that the phonon dispersion plays a critical role in transmission and specularity.

\*\*\*

We acknowledge financial support from a grant from the Science and Engineering Research Council (Grant No. 152-70-00017) and the Agency for Science, Technology, and Research (A\*STAR), Singapore.

## References

- [1] HOCHBAUM A. I., CHEN R., DELGADO R. D., LIANG W., GARNETT E. C., NAJARIAN M., MAJUMDAR A. and YANG P., *Nature*, **451** (2008) 163. <https://doi.org/10.1038/nature06381>
- [2] LIM J., HIPALGAONKAR K., ANDREWS S. C., MAJUMDAR A. and YANG P., *Nano Lett.*, **12** (2012) 2475. <https://doi.org/10.1021/nl3005868>
- [3] LI D. and MCGAUGHEY A. J. H., *Nanoscale Microsc. Thermophys. Eng.*, **19** (2015) 166. <https://doi.org/10.1080/15567265.2015.1035199>

- [4] MONACHON C., WEBER L. and DAMES C., *Annual Review of Materials Research*, **46** (2016) 433.  
<https://doi.org/10.1146/annurev-matsci-070115-031719>
- [5] MAZNEV A. A., *Phys. Rev. B*, **91** (2015) 134306.  
<https://link.aps.org/doi/10.1103/PhysRevB.91.134306>
- [6] RAVICHANDRAN N. K., ZHANG H. and MINNICH A. J., *Phys. Rev. X*, **8** (2018) 41004.  
<https://link.aps.org/doi/10.1103/PhysRevX.8.041004>
- [7] CHEN G., *Nanoscale energy transport and conversion: a parallel treatment of electrons, molecules, phonons, and photons* (Oxford University Press, New York) 2005.
- [8] CHEN G., *Phys. Rev. B*, **57** (1998) 14958.  
<https://link.aps.org/doi/10.1103/PhysRevB.57.14958>
- [9] TERMENTZIDIS K., CHANTRENNE P. and KEBLINSKI P., *Phys. Rev. B*, **79** (2009) 214307.  
<https://link.aps.org/doi/10.1103/PhysRevB.79.214307>
- [10] ZHAO H. and FREUND J. B., *J. Appl. Phys.*, **105** (2009) 13515.  
<https://doi.org/10.1063/1.3054383>
- [11] AKSAMIJA Z. and KNEZEVIC I., *Phys. Rev. B*, **88** (2013) 155318.
- [12] HAO Q., *J. Appl. Phys*, **116** (2014) 034305.  
<https://doi.org/10.1063/1.4890362>
- [13] HUA C. and MINNICH A. J., *Semicond. Sci. Technol.*, **29** (2014) 124004.  
<https://doi.org/10.1088/0268-1242/29/12/124004>
- [14] ZHANG Y., MA D., ZANG Y., WANG X. and YANG N., *Frontiers in Energy Research*, **6** (2018) 48.  
<https://doi.org/10.3389/fenrg.2018.00048>
- [15] SWARTZ E. T. and POHL R. O., *Rev. Mod. Phys.*, **61** (1989) 605.  
<https://link.aps.org/doi/10.1103/RevModPhys.61.605>
- [16] SHI F., LOWE M. and CRASTER R., *Phys. Rev. B*, **95** (2017) 214305.  
<https://link.aps.org/doi/10.1103/PhysRevB.95.214305>
- [17] THORSOS E. I., *J. Acoust. Soc. Am.*, **83** (1988) 78.  
<https://doi.org/10.1121/1.396188>
- [18] LI D., WU Y., KIM P., SHI L., YANG P. and MAJUMDAR A., *Appl. Phys. Lett.*, **83** (2003) 2934.  
<https://doi.org/10.1063/1.1616981>
- [19] LI D., WU Y., FAN R., YANG P. and MAJUMDAR A., *Appl. Phys. Lett.*, **83** (2003) 3186.
- [20] CHEN G., *J. Heat Transfer*, **119** (1997) 220.  
<https://doi.org/10.1115/1.2824212>
- [21] SCHUSTERITSCH G. and PICKARD C. J., *Phys. Rev. B*, **90** (2014) 35424.  
<https://link.aps.org/doi/10.1103/PhysRevB.90.035424>
- [22] ONG Z.-Y., *Phys. Rev. B*, **98** (2018) 195301.  
<https://link.aps.org/doi/10.1103/PhysRevB.98.195301>
- [23] ONG Z. Y., SCHUSTERITSCH G. and PICKARD C. J., *Phys. Rev. B*, **101** (2020) 195410.  
<https://doi.org/10.1103/PhysRevB.101.195410>
- [24] See Supplemental Material at [URL will be inserted by publisher] for [give brief description of material].
- [25] PICKARD C. J. and NEEDS R. J., *Phys. Rev. Lett.*, **97** (2006) 45504.  
<https://link.aps.org/doi/10.1103/PhysRevLett.97.045504>
- [26] TERSOFF J., *Phys. Rev. Lett.*, **61** (1988) 2879.  
<https://link.aps.org/doi/10.1103/PhysRevLett.61.2879>
- [27] LINDSAY L. and BROIDO D. A., *Phys. Rev. B*, **81** (2010) 205441.  
<https://link.aps.org/doi/10.1103/PhysRevB.81.205441>
- [28] GALE J. D. and ROHL A. L., *Mol. Simul.*, **29** (2003) 291.  
<https://doi.org/10.1080/0892702031000104887>
- [29] GAN C. K. C. and ONG Z. Y. Z.-Y., *Journal of Physics Communications*, **5** (2021) 015010.  
<https://doi.org/10.1088/2399-6528/abd8ed>
- [30] MONTHUS C. and GAREL T., *Phys. Rev. B*, **81** (2010) 224208.  
<https://doi.org/10.1103/PhysRevB.81.224208>
- [31] ONG Z.-Y., *J. Appl. Phys*, **124** (2018) 151101.  
<https://doi.org/10.1063/1.5048234>
- [32] ONG Z.-Y. and ZHANG G., *Phys. Rev. B*, **91** (2015) 174302.  
<https://link.aps.org/doi/10.1103/PhysRevB.91.174302>
- [33] SCHELLING P. K., PHILLPOT S. R. and KEBLINSKI P., *Appl. Phys. Lett.*, **80** (2002) 2484.  
<https://doi.org/10.1063/1.1465106>
- [34] SCHELLING P. K., PHILLPOT S. R. and KEBLINSKI P., *J. Appl. Phys.*, **95** (2004) 6082.  
<https://doi.org/10.1063/1.1702100>
- [35] TAN S. H., TANG L. M., XIE Z. X., PAN C. N. and CHEN K. Q., *Carbon*, **65** (2013) 181.  
<https://doi.org/10.1016/j.carbon.2013.08.012>
- [36] HELGEE E. E. and ISACSSON A., *Phys. Rev. B*, **90** (2014) 45416.  
<https://link.aps.org/doi/10.1103/PhysRevB.90.045416>
- [37] XIA J., ZHU Y., WANG F. and WU H., *J. Appl. Phys*, **121** (2017) 215105.  
<https://doi.org/10.1063/1.4984763>

Supplemental material: Specular transmission and diffuse reflection in phonon scattering at grain boundary

Zhun-Yong Ong

*Institute of High Performance Computing, A\*STAR, Singapore 138632, Singapore\**

arXiv:2103.06444v3 [cond-mat.mes-hall] 15 May 2021

---

\* ongzy@ihpc.a-star.edu.sg



## CONTENTS

S1. Grain boundary structure generation and optimization	2
S2. S-matrix calculation methodology	3
S3. Specularity parameters and transmission coefficients for zigzag-edge graphene	6
S4. Low-frequency ZA phonon transmission in ordered GB model (GB-II)	8
References	8

## S1. GRAIN BOUNDARY STRUCTURE GENERATION AND OPTIMIZATION

The generation and optimization of the graphene grain boundary (GB) structures used in our simulation are identical to those in Ref. [1]. The original 186-atom GB-II and GB-III supercells from Ref. [2], which are used to construct the (32,32)|(56,0) GB interfaces, are shown in Fig. S1(a). Each supercell has two (4,4)|(7,0) grain boundaries consisting of a continuous undulating line of pentagon-heptagon defect pairs that define the interface between bulk armchair and zigzag-edge graphene. By ‘zigzag’ or ‘armchair’ edge, we refer to the orientation of the carbon atoms in the  $y$ -direction parallel to the GB.

To generate the larger GB structure in Fig. S1(b), we first expand GB-II and GB-III in the  $x$  direction by increasing the size of the bulk armchair and zigzag-edge graphene region between the two interfaces, to reduce the distortion of the bulk lattice region. We then line  $n_{\text{GB}} = 8$  of the expanded GB-II’s and GB-III’s up in the  $y$ -direction to create the (32,32)|(56,0) GB structure in Fig. S1(b), with the exact configuration of the (32,32)|(56,0) GB depending on the number of GB-II’s and GB-III’s used and the order in which they are arranged.

We model the interatomic interaction using the Tersoff potential [3] with parameters from Ref. [4]. In bulk graphene, the C-C bond length of 1.44Å minimizes the total potential energy. Because the zigzag edge is slightly wider than the armchair edge by about one percent, we use this value to fix the width of the GB as  $L_y = 139.55\text{Å}$  as this results in the minimized average C-C bond length of 1.44Å and 1.45Å in bulk zigzag-edge and armchair-edge graphene, respectively. The slightly longer C-C bond length in armchair-edge graphene is due to the one-percent tensile strain in the  $y$ -direction. We use the code GULP [5] to optimize the atomic positions. The supercell in Fig. S1(b) is allowed to relax only in the  $x$  direction, with periodic boundary conditions are imposed in the  $x$  and  $y$  direction, until the optimized value of  $L_x$ , the length of the supercell in the  $x$ -direction, is obtained. After minimization, the C-C bond lengths in the scattering region bounded by dashed lines in Fig. S1(b) vary between 1.39Å and 1.49Å.

After minimization, the force constants corresponding to the atoms in the scattering region are computed in GULP and then postprocessed to yield the interatomic force constant (IFC) matrix describing the scattering region,

$$\mathbf{K}_C = \begin{pmatrix} \mathbf{K}_{00} & \mathbf{K}_{01} & & \\ \mathbf{K}_{10} & \mathbf{K}_{11} & \mathbf{K}_{12} & \\ & \mathbf{K}_{21} & \mathbf{K}_{22} & \end{pmatrix} \quad (\text{S1})$$

where the submatrix  $\mathbf{K}_{nm}$  describes the coupling between subregions  $n$  and  $m$  in Fig. S1(b). Subregions 0 and 2 represent the bulk-like edges of the scattering region and connect the scattering region to bulk armchair- and zigzag-edge graphene while subregion 1 corresponds to the center of the scattering region. We also extract the matrices  $\mathbf{K}_L^{00}$  and  $\mathbf{K}_L^{01}$  ( $\mathbf{K}_R^{00}$  and  $\mathbf{K}_R^{01}$ ) which describe the coupling within and between layers, as shown in Fig. S1(c), in armchair-edge (zigzag-edge) graphene. The block-tridiagonal IFC matrix for the entire scattering system is

$$\mathbf{K} = \left( \begin{array}{c|cc|cc} \ddots & \ddots & & & & \\ \ddots & \mathbf{K}_L^{00} & & & & \\ \hline & (\mathbf{K}_L^{01})^\dagger & \mathbf{K}_L^{01} & & & \\ & & \mathbf{K}_{00} & \mathbf{K}_{01} & & \\ & & \mathbf{K}_{10} & \mathbf{K}_{11} & \mathbf{K}_{12} & \\ & & & \mathbf{K}_{21} & \mathbf{K}_{22} & \mathbf{K}_R^{01} \\ \hline & & & & (\mathbf{K}_R^{01})^\dagger & \mathbf{K}_R^{00} & \ddots \\ & & & & & \ddots & \ddots \end{array} \right), \quad (\text{S2})$$



between the incoming and outgoing scattering channels which correspond to the bulk phonon modes in armchair and zigzag-edge graphene.

The Green's function of the scattering region in Fig. S1(b) is given by

$$\mathbf{G}_C^{\text{ret}}(\omega) = [(\omega^2 + i0^+)\mathbf{I} - \mathbf{H}_C - \Sigma_L(\omega) - \Sigma_R(\omega)]^{-1}$$

where  $\Sigma_L(\omega) = \mathbf{H}_{\text{CL}}\mathbf{g}_{\text{L},-}^{\text{ret}}(\omega)\mathbf{H}_{\text{CL}}^\dagger$  and  $\Sigma_R(\omega) = \mathbf{H}_{\text{CR}}\mathbf{g}_{\text{R},+}^{\text{ret}}(\omega)\mathbf{H}_{\text{CR}}^\dagger$  are the self-energies associated with the left (i.e. bulk armchair-edge graphene) and right (i.e. bulk zigzag-edge graphene) leads, respectively, with the left and right-lead *retarded* surface Green's functions given by

$$\mathbf{g}_{\text{L},-}^{\text{ret}}(\omega) = [(\omega^2 + i0^+)\mathbf{I}_L - \mathbf{H}_L^{00} - (\mathbf{H}_L^{01})^\dagger \mathbf{g}_{\text{L},-}^{\text{ret}}(\omega)\mathbf{H}_L^{01}]^{-1} \quad (\text{S3a})$$

$$\mathbf{g}_{\text{R},+}^{\text{ret}}(\omega) = [(\omega^2 + i0^+)\mathbf{I}_R - \mathbf{H}_R^{00} - \mathbf{H}_R^{01} \mathbf{g}_{\text{R},+}^{\text{ret}}(\omega)(\mathbf{H}_R^{01})^\dagger]^{-1}. \quad (\text{S3b})$$

$\mathbf{I}$ ,  $\mathbf{I}_L$  and  $\mathbf{I}_R$  are identity matrices of the same size as  $\mathbf{H}_C$ ,  $\mathbf{H}_L^{00}$  and  $\mathbf{H}_R^{00}$ , respectively. In addition, we also define

$$\mathbf{g}_{\text{L},+}^{\text{ret}}(\omega) = [(\omega^2 + i0^+)\mathbf{I}_L - \mathbf{H}_L^{00} - \mathbf{H}_L^{01} \mathbf{g}_{\text{L},+}^{\text{ret}}(\omega)(\mathbf{H}_L^{01})^\dagger]^{-1}, \quad (\text{S3c})$$

$$\mathbf{g}_{\text{R},-}^{\text{ret}}(\omega) = [(\omega^2 + i0^+)\mathbf{I}_R - \mathbf{H}_R^{00} - (\mathbf{H}_R^{01})^\dagger \mathbf{g}_{\text{R},-}^{\text{ret}}(\omega)\mathbf{H}_R^{01}]^{-1}, \quad (\text{S3d})$$

$\mathbf{g}_{\text{L},-}^{\text{adv}}(\omega) = \mathbf{g}_{\text{L},-}^{\text{ret}}(\omega)^\dagger$  and  $\mathbf{g}_{\text{R},+}^{\text{adv}}(\omega) = \mathbf{g}_{\text{R},+}^{\text{ret}}(\omega)^\dagger$ . The retarded surface Green's functions in Eq. (S3) can be computed using established numerical methods [7] and exploiting the transverse translational symmetry [6].

Given Eq. (S3), we define the Bloch matrices ( $\mathbf{F}_L^{\text{ret/adv}}(-)$  and  $\mathbf{F}_R^{\text{ret/adv}}(+)$ ):

$$\mathbf{F}_L^{\text{ret/adv}}(-)^{-1} = \mathbf{g}_{\text{L},-}^{\text{ret/adv}} \mathbf{H}_L^{01}$$

$$\mathbf{F}_R^{\text{ret/adv}}(+) = \mathbf{g}_{\text{R},+}^{\text{ret/adv}} \mathbf{H}_R^{10}$$

and their associated eigenmode matrices ( $\mathbf{U}_L^{\text{ret/adv}}(-)$  and  $\mathbf{U}_R^{\text{ret/adv}}(+)$ ):

$$\mathbf{F}_L^{\text{ret/adv}}(-)^{-1} \mathbf{U}_L^{\text{ret/adv}}(-) = \mathbf{U}_L^{\text{ret/adv}}(-) \mathbf{\Lambda}_L^{\text{ret/adv}}(-)^{-1} \quad (\text{S4a})$$

$$\mathbf{F}_R^{\text{ret/adv}}(+) \mathbf{U}_R^{\text{ret/adv}}(+) = \mathbf{U}_R^{\text{ret/adv}}(+) \mathbf{\Lambda}_R^{\text{ret/adv}}(+) \quad (\text{S4b})$$

along with the eigenvelocity matrices ( $\mathbf{V}_L^{\text{ret/adv}}(-)$  and  $\mathbf{V}_R^{\text{ret/adv}}(+)$ ):

$$\mathbf{V}_L^{\text{ret/adv}}(-) = -\frac{ia_L}{2\omega} [\mathbf{U}_L^{\text{ret/adv}}(-)]^\dagger \mathbf{H}_L^{10} [\mathbf{g}_{\text{L},-}^{\text{ret/adv}} - (\mathbf{g}_{\text{L},-}^{\text{ret/adv}})^\dagger] \mathbf{H}_L^{01} \mathbf{U}_L^{\text{ret/adv}}(-) \quad (\text{S5a})$$

$$\mathbf{V}_R^{\text{ret/adv}}(+) = \frac{ia_R}{2\omega} [\mathbf{U}_R^{\text{ret/adv}}(+)]^\dagger \mathbf{H}_R^{01} [\mathbf{g}_{\text{R},+}^{\text{ret/adv}} - (\mathbf{g}_{\text{R},+}^{\text{ret/adv}})^\dagger] \mathbf{H}_R^{10} \mathbf{U}_R^{\text{ret/adv}}(+) \quad (\text{S5b})$$

Dropping the subscripts and superscripts, we can write the eigenmode matrices in Eq. (S4) as

$$\mathbf{U} = (\mathbf{u}(\mathbf{k}_1), \mathbf{u}(\mathbf{k}_2), \dots, \mathbf{u}(\mathbf{k}_N)) \quad (\text{S6})$$

where  $\mathbf{u}(\mathbf{k}_n)$  is a column vector corresponding to the phonon eigenmode with wave vector  $\mathbf{k}_n$  which is real for bulk phonon modes and complex for evanescent modes. The wave vector  $\mathbf{k}_n$  is determined using the zone-unfolding procedure described in Ref. [6] and is also identified according to its polarization/branch. We may regard each column vector of  $\mathbf{U}_L^{\text{adv}}(-)$  [ $\mathbf{U}_L^{\text{ret}}(-)$ ] as an incoming (outgoing) left-lead phonon mode describing the atomic displacements in the bulk layer immediately left of subregion 0 in Fig. S1(b) and likewise each column vector of  $\mathbf{U}_R^{\text{adv}}(+)$  [ $\mathbf{U}_R^{\text{ret}}(+)$ ] as an incoming (outgoing) right-lead phonon mode describing the atomic displacements in the bulk layer immediately right of subregion 2 in Fig. S1(a). Although there are  $N$  column vectors on the right hand side of Eq. (S6) at each frequency  $\omega$ , only a subset of them correspond to bulk phonon modes, with the number of bulk phonon modes varying with the frequency.

In the following discussion, we reserve the symbols  $\mathbf{p}_n$  and  $\mathbf{p}'_n$  (where  $n = 1, \dots, N_L(\omega)$  and  $N_L(\omega)$  is the number of outgoing or incoming phonon modes at frequency  $\omega$ ) for the wave vectors of the outgoing and incoming *left*-lead bulk phonons, respectively, and  $\mathbf{q}_m$  and  $\mathbf{q}'_m$  (where  $m = 1, \dots, N_R(\omega)$  and  $N_R(\omega)$  is the number of outgoing or incoming *right*-lead phonon modes at frequency  $\omega$ ) for the wave vectors of the outgoing and incoming right-lead bulk phonons, respectively. The incoming bulk phonon modes are marked with a  $\prime$  superscript while the outgoing ones are not. At each frequency  $\omega$ , we have a set of outgoing left-lead phonons associated with the wave vectors  $\mathcal{U}_L^{\text{ret}}(\omega) = \{\mathbf{p}_1, \dots, \mathbf{p}_{N_L(\omega)}\}$ . The number of elements as well as the composition of this set depends on  $\omega$ . So, at another frequency  $\omega' \neq \omega$ , we have a different set of left-lead phonons  $\mathcal{U}_L^{\text{ret}}(\omega') = \{\mathbf{p}_1, \dots, \mathbf{p}_{N_L(\omega')}\}$  and its wave vectors are usually different to those of  $\mathcal{U}(\omega)$  unless the phonons belong to different polarization branches. Therefore, at each frequency  $\omega$ , we have two sets of wave vectors  $\mathcal{U}_L^{\text{adv}}(\omega) = \{\mathbf{p}'_1, \dots, \mathbf{p}'_{N_L(\omega)}\}$  and  $\mathcal{U}_R^{\text{adv}}(\omega) = \{\mathbf{q}'_1, \dots, \mathbf{q}'_{N_R(\omega)}\}$  associated with the incoming left and right-lead phonons, respectively, and another two sets of wave vectors  $\mathcal{U}_L^{\text{ret}}(\omega) = \{\mathbf{p}_1, \dots, \mathbf{p}_{N_L(\omega)}\}$  and  $\mathcal{U}_R^{\text{ret}}(\omega) = \{\mathbf{q}_1, \dots, \mathbf{q}_{N_R(\omega)}\}$  associated with the outgoing left and right-lead phonons, respectively.

Given Eqs. (S4) and (S5), the formulas for the transmission and reflection matrices are: [6]

$$\mathbf{t}_{\text{RL}}(\omega) = \frac{2i\omega}{\sqrt{a_{\text{R}}a_{\text{L}}}} [\mathbf{V}_{\text{R}}^{\text{ret}}(+)]^{1/2} [\mathbf{U}_{\text{R}}^{\text{ret}}(+)]^{-1} \mathbf{G}_{\text{RL}}^{\text{ret}} [\mathbf{U}_{\text{L}}^{\text{adv}}(-)^\dagger]^{-1} [\mathbf{V}_{\text{L}}^{\text{adv}}(-)]^{1/2} \quad (\text{S7a})$$

$$\mathbf{t}_{\text{LR}}(\omega) = \frac{2i\omega}{\sqrt{a_{\text{L}}a_{\text{R}}}} [\mathbf{V}_{\text{L}}^{\text{ret}}(-)]^{1/2} [\mathbf{U}_{\text{L}}^{\text{ret}}(-)]^{-1} \mathbf{G}_{\text{LR}}^{\text{ret}} [\mathbf{U}_{\text{R}}^{\text{adv}}(+)\dagger]^{-1} [\mathbf{V}_{\text{R}}^{\text{adv}}(+)]^{1/2} \quad (\text{S7b})$$

$$\mathbf{r}_{\text{LL}}(\omega) = \frac{2i\omega}{a_{\text{L}}} [\mathbf{V}_{\text{L}}^{\text{ret}}(-)]^{1/2} [\mathbf{U}_{\text{L}}^{\text{ret}}(-)]^{-1} (\mathbf{G}_{\text{L}}^{\text{ret}} - \mathbf{Q}_{\text{L}}^{-1}) [\mathbf{U}_{\text{L}}^{\text{adv}}(-)^\dagger]^{-1} [\mathbf{V}_{\text{L}}^{\text{adv}}(-)]^{1/2} \quad (\text{S7c})$$

$$\mathbf{r}_{\text{RR}}(\omega) = \frac{2i\omega}{a_{\text{R}}} [\mathbf{V}_{\text{R}}^{\text{ret}}(+)]^{1/2} [\mathbf{U}_{\text{R}}^{\text{ret}}(+)]^{-1} (\mathbf{G}_{\text{R}}^{\text{ret}} - \mathbf{Q}_{\text{R}}^{-1}) [\mathbf{U}_{\text{R}}^{\text{adv}}(+)\dagger]^{-1} [\mathbf{V}_{\text{R}}^{\text{adv}}(+)]^{1/2} \quad (\text{S7d})$$

where

$$\mathbf{G}_{\text{RL}}^{\text{ret}}(\omega) = \mathbf{g}_{\text{R},+}^{\text{ret}}(\omega) \mathbf{H}_{\text{RC}} \mathbf{G}_{\text{C}}^{\text{ret}}(\omega) \mathbf{H}_{\text{CL}} \mathbf{g}_{\text{L},-}^{\text{ret}}(\omega)$$

$$\mathbf{G}_{\text{LR}}^{\text{ret}}(\omega) = \mathbf{g}_{\text{L},-}^{\text{ret}}(\omega) \mathbf{H}_{\text{LC}} \mathbf{G}_{\text{C}}^{\text{ret}}(\omega) \mathbf{H}_{\text{CR}} \mathbf{g}_{\text{R},+}^{\text{ret}}(\omega)$$

$$\mathbf{G}_{\text{L}}^{\text{ret}}(\omega) = \mathbf{g}_{\text{L},-}^{\text{ret}}(\omega) + \mathbf{g}_{\text{L},-}^{\text{ret}}(\omega) \mathbf{H}_{\text{LC}} \mathbf{G}_{\text{C}}^{\text{ret}}(\omega) \mathbf{H}_{\text{CL}} \mathbf{g}_{\text{L},-}^{\text{ret}}(\omega)$$

$$\mathbf{G}_{\text{R}}^{\text{ret}}(\omega) = \mathbf{g}_{\text{R},+}^{\text{ret}}(\omega) + \mathbf{g}_{\text{R},+}^{\text{ret}}(\omega) \mathbf{H}_{\text{RC}} \mathbf{G}_{\text{C}}^{\text{ret}}(\omega) \mathbf{H}_{\text{CR}} \mathbf{g}_{\text{R},+}^{\text{ret}}(\omega)$$

$$\mathbf{Q}_{\text{L}}(\omega) = (\omega^2 + i0^+) \mathbf{I}_{\text{L}} - \mathbf{H}_{\text{L}}^{00} - (\mathbf{H}_{\text{L}}^{01})^\dagger \mathbf{g}_{\text{L},-}^{\text{ret}}(\omega) \mathbf{H}_{\text{L}}^{01} - \mathbf{H}_{\text{L}}^{01} \mathbf{g}_{\text{L},+}^{\text{ret}}(\omega) (\mathbf{H}_{\text{L}}^{01})^\dagger$$

$$\mathbf{Q}_{\text{R}}(\omega) = (\omega^2 + i0^+) \mathbf{I}_{\text{R}} - \mathbf{H}_{\text{R}}^{00} - (\mathbf{H}_{\text{R}}^{01})^\dagger \mathbf{g}_{\text{R},-}^{\text{ret}}(\omega) \mathbf{H}_{\text{R}}^{01} - \mathbf{H}_{\text{R}}^{01} \mathbf{g}_{\text{R},+}^{\text{ret}}(\omega) (\mathbf{H}_{\text{R}}^{01})^\dagger$$

We obtain the reduced transmission and reflection matrices  $\bar{\mathbf{t}}_{\text{RL}}$ ,  $\bar{\mathbf{t}}_{\text{LR}}$ ,  $\bar{\mathbf{r}}_{\text{LL}}$  and  $\bar{\mathbf{r}}_{\text{RR}}$  from Eq. (S7) by eliminating the matrix columns and rows associated with the evanescent modes. The matrix  $\bar{\mathbf{t}}_{\text{RL}}$  is an  $N_{\text{R}} \times N_{\text{L}}$  matrix of the form:

$$\bar{\mathbf{t}}_{\text{RL}} = \begin{pmatrix} S(\mathbf{q}_1, \mathbf{p}'_1) & \dots & S(\mathbf{q}_1, \mathbf{p}'_{N_{\text{L}}}) \\ \vdots & \ddots & \vdots \\ S(\mathbf{q}_{N_{\text{R}}}, \mathbf{p}'_1) & \dots & S(\mathbf{q}_{N_{\text{R}}}, \mathbf{p}'_{N_{\text{L}}}) \end{pmatrix} \quad (\text{S9})$$

where  $S(\mathbf{q}_n, \mathbf{p}'_m)$  is the complex scattering amplitude between the incoming left-lead  $\mathbf{p}'_m$  phonon mode and the outgoing right-lead  $\mathbf{q}_n$  phonon mode. Similarly, the remaining transmission and reflection matrices are

$$\bar{\mathbf{r}}_{\text{LL}} = \begin{pmatrix} S(\mathbf{p}_1, \mathbf{p}'_1) & \dots & S(\mathbf{p}_1, \mathbf{p}'_{N_{\text{L}}}) \\ \vdots & \ddots & \vdots \\ S(\mathbf{p}_{N_{\text{L}}}, \mathbf{p}'_1) & \dots & S(\mathbf{p}_{N_{\text{L}}}, \mathbf{p}'_{N_{\text{L}}}) \end{pmatrix} \quad (\text{S10})$$



$$\bar{\mathbf{t}}_{\text{LR}} = \begin{pmatrix} S(\mathbf{p}_1, \mathbf{q}'_1) & \cdots & S(\mathbf{p}_1, \mathbf{q}'_{N_{\text{R}}}) \\ \vdots & \ddots & \vdots \\ S(\mathbf{p}_{N_{\text{L}}}, \mathbf{q}'_1) & \cdots & S(\mathbf{p}_{N_{\text{L}}}, \mathbf{q}'_{N_{\text{R}}}) \end{pmatrix} \quad (\text{S11})$$

$$\bar{\mathbf{r}}_{\text{RR}} = \begin{pmatrix} S(\mathbf{q}_1, \mathbf{q}'_1) & \cdots & S(\mathbf{q}_1, \mathbf{q}'_{N_{\text{L}}}) \\ \vdots & \ddots & \vdots \\ S(\mathbf{q}_{N_{\text{R}}}, \mathbf{q}'_1) & \cdots & S(\mathbf{q}_{N_{\text{R}}}, \mathbf{q}'_{N_{\text{L}}}) \end{pmatrix} \quad (\text{S12})$$

Equations (S9) to (S12) are combined to yield the overall  $N_{\text{S}} \times N_{\text{S}}$  scattering matrix:

$$\mathbf{S}(\omega) = \begin{pmatrix} \bar{\mathbf{r}}_{\text{LL}} & \bar{\mathbf{t}}_{\text{LR}} \\ \bar{\mathbf{t}}_{\text{RL}} & \bar{\mathbf{r}}_{\text{RR}} \end{pmatrix} = \left( \begin{array}{ccc|ccc} S(\mathbf{p}_1, \mathbf{p}'_1) & \cdots & S(\mathbf{p}_1, \mathbf{p}'_{N_{\text{L}}}) & S(\mathbf{p}_1, \mathbf{q}'_1) & \cdots & S(\mathbf{p}_1, \mathbf{q}'_{N_{\text{R}}}) \\ \vdots & \ddots & \vdots & \vdots & \ddots & \vdots \\ S(\mathbf{p}_{N_{\text{L}}}, \mathbf{p}'_1) & \cdots & S(\mathbf{p}_{N_{\text{L}}}, \mathbf{p}'_{N_{\text{L}}}) & S(\mathbf{p}_{N_{\text{L}}}, \mathbf{q}'_1) & \cdots & S(\mathbf{p}_{N_{\text{L}}}, \mathbf{q}'_{N_{\text{R}}}) \\ \hline S(\mathbf{q}_1, \mathbf{p}'_1) & \cdots & S(\mathbf{q}_1, \mathbf{p}'_{N_{\text{L}}}) & S(\mathbf{q}_1, \mathbf{q}'_1) & \cdots & S(\mathbf{q}_1, \mathbf{q}'_{N_{\text{R}}}) \\ \vdots & \ddots & \vdots & \vdots & \ddots & \vdots \\ S(\mathbf{q}_{N_{\text{R}}}, \mathbf{p}'_1) & \cdots & S(\mathbf{q}_{N_{\text{R}}}, \mathbf{p}'_{N_{\text{L}}}) & S(\mathbf{q}_{N_{\text{R}}}, \mathbf{q}'_1) & \cdots & S(\mathbf{q}_{N_{\text{R}}}, \mathbf{q}'_{N_{\text{R}}}) \end{array} \right), \quad (\text{S13})$$

satisfying the unitary condition

$$\mathbf{S}(\omega)\mathbf{S}(\omega)^\dagger = \mathbf{S}(\omega)^\dagger\mathbf{S}(\omega) = \mathbf{I}_{\text{S}}$$

where  $N_{\text{S}} = N_{\text{L}} + N_{\text{R}}$  and  $\mathbf{I}_{\text{S}}$  is the  $N_{\text{S}} \times N_{\text{S}}$  scattering matrix. Equation (S13) can be expressed as:

$$\mathbf{S}(\omega) = \begin{pmatrix} S(\mathbf{k}_1, \mathbf{k}'_1) & \cdots & S(\mathbf{k}_1, \mathbf{k}'_{N_{\text{S}}}) \\ \vdots & \ddots & \vdots \\ S(\mathbf{k}_{N_{\text{S}}}, \mathbf{k}'_1) & \cdots & S(\mathbf{k}_{N_{\text{S}}}, \mathbf{k}'_{N_{\text{S}}}) \end{pmatrix}$$

where we have combined the left and right-lead wave vectors such that for  $n = 1, \dots, N_{\text{S}}$ ,

$$\mathbf{k}_n = \begin{cases} \mathbf{p}_n & , n \leq N_{\text{L}} \\ \mathbf{q}_{n-N_{\text{L}}} & , N_{\text{L}} < n \leq N_{\text{S}} \end{cases}.$$

From Eq. (S13), we define the transition probability matrix  $\mathbf{W}(\omega)$

$$\mathbf{W}(\omega) = \begin{pmatrix} W(\mathbf{k}_1, \mathbf{k}'_1) & \cdots & W(\mathbf{k}_1, \mathbf{k}'_{N_{\text{S}}}) \\ \vdots & \ddots & \vdots \\ W(\mathbf{k}_{N_{\text{S}}}, \mathbf{k}'_1) & \cdots & W(\mathbf{k}_{N_{\text{S}}}, \mathbf{k}'_{N_{\text{S}}}) \end{pmatrix} \quad (\text{S14})$$

where each matrix element of  $\mathbf{W}(\omega)$  is equal to the absolute square of the corresponding matrix element of  $\mathbf{S}(\omega)$ , e.g.  $W(\mathbf{k}_n, \mathbf{k}'_m) = |S(\mathbf{k}_n, \mathbf{k}'_m)|^2$ .

### S3. SPECULARITY PARAMETERS AND TRANSMISSION COEFFICIENTS FOR ZIGZAG-EDGE GRAPHENE

The specularity parameters (total, transmission and reflection) and the transmission coefficients for zigzag-edge graphene in the disordered GB model are shown in Fig. S2.

The specularity parameters (total, transmission and reflection) and the transmission coefficients for zigzag-edge graphene in the ordered GB model (GB-II only) are shown in Fig. S3.

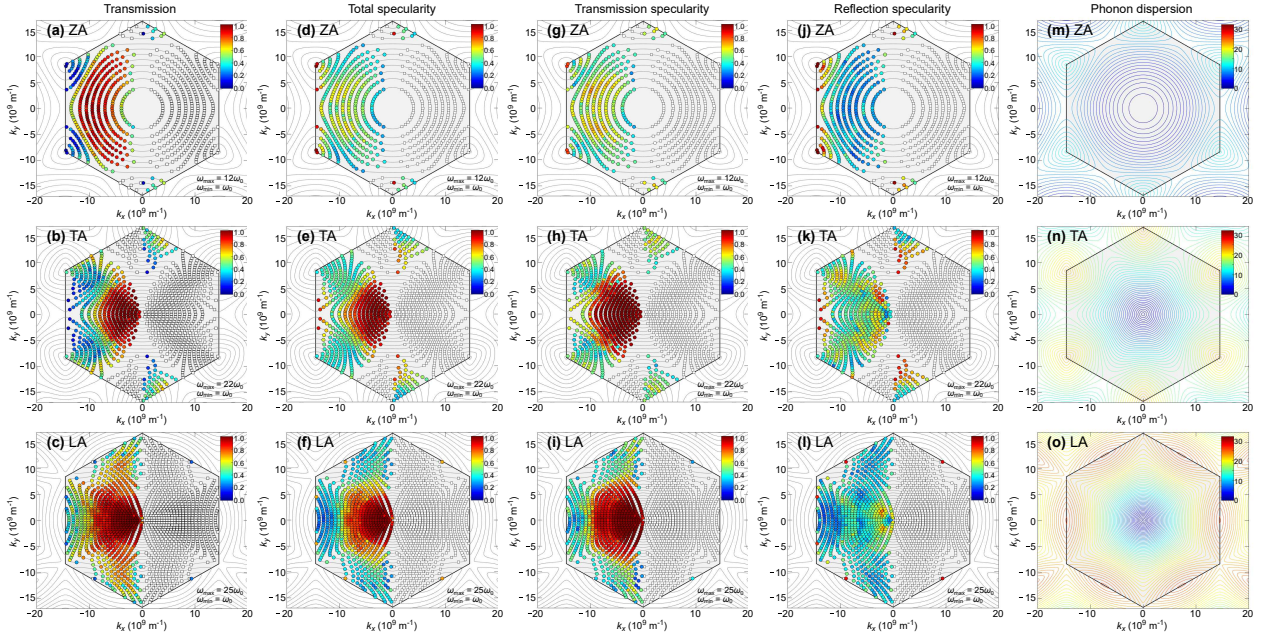


Figure S2. Mode-resolved comparison of (a-c)  $\mathcal{T}_n(\omega)$ , (d-f)  $P_n^{\text{total}}(\omega)$ , (g-i)  $P_n^+(\omega)$ , and (j-l)  $P_n^-(\omega)$  for ZA, TA and LA phonons in zigzag-edge graphene at each frequency  $\omega$  point over the frequency range  $\omega = m\omega_0$  for  $m = 1$  to 25 and  $\omega_0 = 10^{13}$  rad/s (6.58 meV). The isofrequency contours at each  $\omega$  are shown using solid gray lines. The modes in the incoming phonon flux are represented by filled circles, colored according to their numerical value as indicated in the color bars, while the modes in the outgoing flux are represented by hollow squares. The (m) ZA, (n) TA and (o) LA phonon dispersions are indicated with color contours in intervals of  $\Delta\omega = \omega_0/2$ .

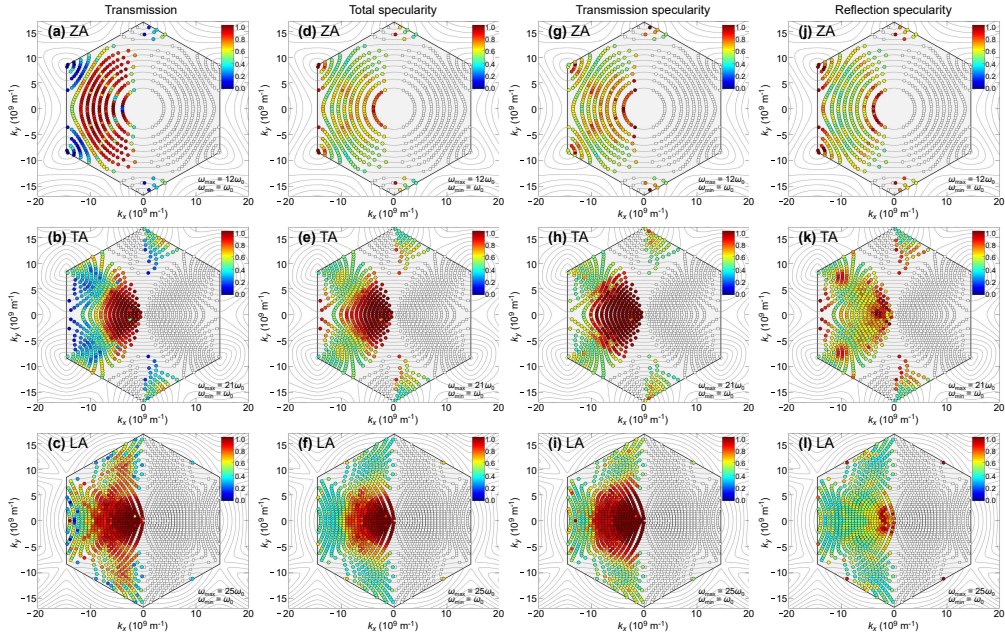


Figure S3. Mode-resolved comparison of (a-c)  $\mathcal{T}_n(\omega)$ , (d-f)  $P_n^{\text{total}}(\omega)$ , (g-i)  $P_n^+(\omega)$ , and (j-l)  $P_n^-(\omega)$  for ZA, TA and LA phonons in zigzag-edge graphene at each frequency  $\omega$  point over the frequency range  $\omega = m\omega_0$  for  $m = 1$  to 25 and  $\omega_0 = 10^{13}$  rad/s (6.58 meV) for a (32,32)|(56,0) graphene GB constructed from only GB-II subunits. The isofrequency contours at each  $\omega$  are shown using solid gray lines. The modes in the incoming phonon flux are represented by filled circles, colored according to their numerical value as indicated in the color bars, while the modes in the outgoing flux are represented by hollow squares.

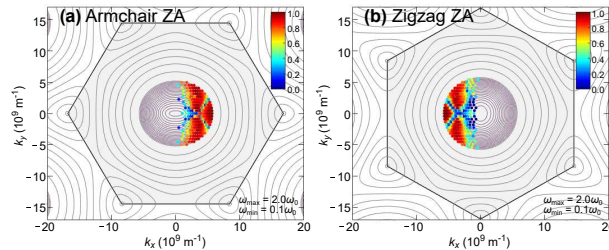


Figure S4. Mode-resolved comparison of  $\mathcal{T}_n(\omega)$  in the low-frequency regime for ZA phonons in **(a)** armchair and **(b)** zigzag-edge graphene at each frequency  $\omega$  point over the frequency range  $\omega = 0.1\omega_0$  to  $2\omega_0$  for  $\omega_0 = 10^{13}$  rad/s (6.58 meV) with a frequency step size of  $0.1\omega_0$  for a  $(32,32)|(56,0)$  graphene GB constructed from only GB-II subunits. The isofrequency contours at each  $\omega$  at and under  $\omega = 2\omega_0$  are displayed using solid magenta lines at intervals of  $\Delta\omega = 0.1\omega_0$  while the isofrequency contours between  $\omega = 2\omega_0$  and  $\omega = 12\omega_0$  are displayed using solid gray lines at intervals of  $\Delta\omega = \omega_0$ . The modes in the incoming phonon flux are represented by filled circles, colored according to their numerical value as indicated in the color bars.

#### S4. LOW-FREQUENCY ZA PHONON TRANSMISSION IN ORDERED GB MODEL (GB-II)

In Fig. S4, we plot the low-frequency ZA phonon transmission coefficients in armchair and zigzag-edge graphene for a  $(32,32)|(56,0)$  graphene GB constructed from only GB-II subunits.

- 
- [1] Z. Y. Ong, G. Schusteritsch, and C. J. Pickard, Phys. Rev. B **101**, 195410 (2020), arXiv:2004.07424.
  - [2] G. Schusteritsch and C. J. Pickard, Phys. Rev. B **90**, 35424 (2014).
  - [3] J. Tersoff, Phys. Rev. Lett. **61**, 2879 (1988).
  - [4] L. Lindsay and D. A. Broido, Phys. Rev. B **81**, 205441 (2010).
  - [5] J. D. Gale and A. L. Rohl, Mol. Simul. **29**, 291 (2003).
  - [6] Z.-Y. Ong, Phys. Rev. B **98**, 195301 (2018).
  - [7] J.-S. Wang, J. Wang, and J. T. Lü, Eur. Phys. J. B **62**, 381 (2008).